



UNIVERSITY OF LEEDS

This is a repository copy of *The Dynamic Expulsion of Magnetic Flux by Vortices*.

White Rose Research Online URL for this paper:

<https://eprints.whiterose.ac.uk/225661/>

Version: Accepted Version

Article:

Tessier, J., Poulin, F.J. and Hughes, D.W. orcid.org/0000-0002-8004-8631 (Accepted: 2025) *The Dynamic Expulsion of Magnetic Flux by Vortices*. *Physical Review Fluids* (PRFluids). ISSN 2469-990X (In Press)

This is an author produced version of an article accepted for publication in *Physical Review Fluids*, made available under the terms of the Creative Commons Attribution License (CC-BY), which permits unrestricted use, distribution and reproduction in any medium, provided the original work is properly cited.

Reuse

This article is distributed under the terms of the Creative Commons Attribution (CC BY) licence. This licence allows you to distribute, remix, tweak, and build upon the work, even commercially, as long as you credit the authors for the original work. More information and the full terms of the licence here:

<https://creativecommons.org/licenses/>

Takedown

If you consider content in White Rose Research Online to be in breach of UK law, please notify us by emailing eprints@whiterose.ac.uk including the URL of the record and the reason for the withdrawal request.



eprints@whiterose.ac.uk
<https://eprints.whiterose.ac.uk/>

The Dynamic Expulsion of Magnetic Flux by Vortices

Jonathan Tessier*

Institut des sciences de la mer de Rimouski, Université du Québec à Rimouski, Rimouski, QC, Canada, G5L 3A1

Francis J. Poulin†

Department of Applied Mathematics, University of Waterloo, Waterloo, ON, Canada, N2L 3G1

David W. Hughes‡

Department of Applied Mathematics, University of Leeds, Leeds LS2 9JT, UK

(Dated: April 22, 2025)

We study numerically the dynamical evolution of two different vorticity arrays with an initially uniform magnetic field in two-dimensional incompressible magnetohydrodynamics. We concentrate particularly on the role of the strength of the background magnetic field, which is always assumed weak in the sense that its energy is much less than the kinetic energy of the vortical flows. Within the context of a weak background field, we are able to identify four distinct regimes. When the field is so weak that the back-reaction of the Lorentz force can be ignored (the kinematic regime), classical flux expulsion occurs. As the field strength is increased, the first signs of the dynamical influence of the small-scale field generated is in the disruption of vortex filaments, with flux expulsion still occurring in the vortex cores. A further increase in field strength leads to the regime of vortex disruption, in which the magnetic field is expelled, but is then of sufficient strength to disrupt or destroy the vortices. For yet stronger fields, even the large-scale field can be sufficiently strong to be dynamically active; flux expulsion is then prevented and the field is dynamically active throughout the evolution. Furthermore, in the case of a row of vortices, we show that the orientation of the background field significantly influences the evolution, especially at higher field strengths.

I. INTRODUCTION

The process of flux expulsion, in which magnetic field is expelled from circulating eddies, is a widely studied phenomenon, with implications for the concentration of magnetic fields by swirling convective motions in stellar and planetary interiors (see, for example, [1–3]).

Flux expulsion was first addressed in the pioneering study of Weiss [1] (see also [4]), who considered the kinematic evolution of an initially uniform magnetic field in a variety of steady, two-dimensional cellular flows. Weiss demonstrated how magnetic flux is initially concentrated at the edges of the cells and amplified within the eddy, before a period of reconnection, in which the central field decays and the configuration relaxes to a steady state. Through a combination of physical arguments and numerical simulations, Weiss established the dependence of the magnetic energy and the timescale for expulsion on the magnetic Reynolds number Rm , defined by $Rm = U_0 L / \eta$, where U_0 and L are characteristic velocity and length scales, and η is the magnetic diffusivity. For an initial field of strength B_0 , and assuming Rm to be large, the peak field strength B_1 satisfies $B_1^2 \sim Rm^{2/3} B_0^2$, while the strength of the final steady state field B_2 satisfies $B_2^2 \sim Rm^{1/3} B_0^2$; the timescale associated with the process of flux expulsion is $O(Rm^{1/3} T_0)$, where T_0 is a characteristic flow timescale (see also [5, 6]).

The studies [1, 5, 6] addressed the problem of the kinematic evolution of the magnetic field, in which the back-reaction of the field on the flow via the Lorentz force is neglected. In the dynamical evolution, in which the Lorentz force is incorporated, one of the most interesting issues concerns the strength of the initial field B_0 at which the dynamic and kinematic evolutions markedly differ. Mak et al. [7], building on the work of Ref. [8], argued theoretically that dynamic effects could become important, leading to vortex disruption, provided that

$$M^2 Rm \sim 1, \quad (1)$$

where M^2 denotes the ratio of the initial magnetic energy to the kinetic energy of the flow. This critical field strength for disruption was then confirmed by numerical simulations of the nonlinear evolution of vortices emerging from the instabilities of parallel shear flows in the presence of a weak background field [7]. The incorporation of dynamical effects into the process of flux expulsion has also been considered in Ref. [9] via a quasi-linear analysis in which only the axisymmetric component of the Lorentz force is retained, thereby leading to a slightly different scaling to that derived in [7]. It is noteworthy that the scaling (1) implies that for high values of Rm , only a very weak background field (small M^2) is needed for the Lorentz force to play a significant role; although the field is weak on the large scale, it is greatly amplified on the small scale so as to become dynamically significant. Such behavior is important in an astrophysical context, where Rm is invariably high, and has been previously identified in the suppression of turbulent transport [10–16], in the suppression of jets in β -plane turbulence [17], and in

* jonathan.tessier@uqar.ca

† fpoulin@uwaterloo.ca

‡ d.w.hughes@leeds.ac.uk

the inhibition of large-scale vortex formation in rapidly rotating convection [18].

Weiss [1] considered a variety of flow patterns, which can be classified, broadly speaking, as having either a single cell or a band of eddies. Most studies of flux expulsion — both kinematic and dynamic — have focused on the case of a single isolated cell. Our aim in this paper therefore is to concentrate on the problem of flux expulsion in connected vortices, and, specifically, to extend the kinematic studies into the dynamic regime.

A related study [19], at lower resolution and lower Reynolds numbers, focuses on the effect of turbulent fluctuations to the spatial distribution of the magnetic potential in a quasi-stationary state. While Ref. [19] considers a forced array of vortices in a sinusoidal background field, we focus on high Reynolds number run-down experiments of various arrangements of vortices in a uniform background field of varying strength.

The paper is organized as follows. In section II we present the mathematical formulation of the problem, which includes the governing equations and the different sets of initial conditions. Three vortex arrangements are considered: a row of vortices aligned with the field, one perpendicular to it, and a two by two periodic tile of vortices. Next, in section III, we discuss the numerical methods used in our simulations and the associated diagnostics employed to determine important features of the flow and magnetic field. Section IV presents the results of the simulations, where each configuration is tested with four different magnetic field strengths: a kinematic field, a very weak dynamical field, a critical field strength, and a strong field. The impact of the field strength and direction on flux expulsion is analyzed through various diagnostics. We conclude with a discussion in section V.

II. MATHEMATICAL FORMULATION

We investigate the dynamics of two-dimensional, incompressible magnetohydrodynamics (MHD), with the magnetic field in the plane of the fluid motion. We implicitly scale the magnetic field by a factor of $1/\sqrt{\mu_0\rho}$, with μ_0 the magnetic permeability of the fluid and ρ the (constant) density, such that the field has units of velocity. The velocity \mathbf{u} is expressed in terms of a stream function ψ , and the magnetic field \mathbf{b} in terms of a background magnetic flux function \bar{A} and associated perturbation A . The vorticity and electric current have a non-zero component only in the z -direction; they are denoted, respectively, by q and j . The governing equations may be expressed as evolution equations for q and A . The flow has a characteristic speed U_0 and a characteristic length scale L ; there is a background uniform magnetic field of strength B_0 . We thus scale lengths with L , time with an advective time scale L/U_0 , and magnetic field with B_0 . In non-dimensional form, the governing equations then

become

$$\partial_t q + \mathbf{u} \cdot \nabla q = M^2 \mathbf{b} \cdot \nabla j + Re^{-1} \nabla^2 q, \quad (2a)$$

$$\partial_t A + \mathbf{u} \cdot \nabla (A + \bar{A}) = Rm^{-1} \nabla^2 A, \quad (2b)$$

$$\mathbf{u} = \hat{z} \times \nabla \psi, \quad \mathbf{b} = \hat{z} \times \nabla (A + \bar{A}), \quad (2c)$$

$$q = \nabla^2 \psi, \quad j = \nabla^2 A, \quad (2d)$$

where

$$M = \frac{B_0}{U_0}, \quad Re = \frac{U_0 L}{\nu}, \quad Rm = \frac{U_0 L}{\eta}, \quad (3)$$

with ν the kinematic viscosity and η the magnetic diffusivity (both constants). Here $\bar{A}(x, y)$ is the flux function of the uniform background magnetic field; for a field in the x (y) direction, \bar{A} is a linear function of y (x) (and hence $\nabla^2 \bar{A} = 0$). The problem is described by the three dimensionless parameters in Eqs. (3): M is the ratio of the strength of the (scaled) background field (the Alfvén wave speed) to the typical flow speed; Re and Rm are, respectively, the fluid and magnetic Reynolds numbers.

We solve Eqs. (2) as an initial value problem for a prescribed velocity with an initially uniform magnetic field. These are rundown experiments, where the initial conditions are set and allowed to evolve under no additional forcing. Though viscosity influences the motion, the evolution to the final stationary state is inherently very slow when the fluids Reynolds number is high. We assume periodic boundary conditions in both the x and y -directions for both evolved quantities, q and A , on a square domain.

Inspired by the original examples from [1], we study two types of vortex configurations as initial conditions. The first comprises a single row of vortices with alternating polarity on a domain with edges of length 8π , $0 < x, y < 8\pi$, with vorticity defined by

$$q_{row} = \begin{cases} -\sin\left(\frac{x}{2}\right) \cos\left(\frac{y}{2}\right), & |y - 4\pi| < \pi \\ 0, & \text{otherwise.} \end{cases} \quad (4)$$

Note that this profile differs from that studied in [1], in that instead of specifying the streamfunction we specify the vorticity. In the region where the vorticity is non-zero, the two approaches are identical. However, we have chosen to specify the vorticity patchwise, as this then guarantees that the associated velocity and streamfunction are smooth in the continuous limit. We do not believe that there should be any significant differences between the two approaches, but we have not investigated this in detail. This centered row of vortices spans a quarter of the y -domain, and hence the flow is anisotropic. We therefore investigate (as did Weiss) the distinct cases in which the background uniform magnetic field is in the x -direction and the y -direction.

The second type of initial vortex configuration that we consider is a two by two tile of vortices of the same size as the previous case, and which thus fit exactly in a square domain with edges of length 4π , $0 < x, y < 4\pi$. The

vorticity takes the form

$$q_{tile} = -\sin\left(\frac{x}{2}\right)\sin\left(\frac{y}{2}\right), \quad (5)$$

and is an exact solution to the system (2) in the inviscid ($Re \rightarrow \infty$) and hydrodynamic ($M = 0$) limit. In this case, the symmetry of the initial conditions makes the direction of the background field irrelevant (with regard to the x and y -directions), and so we will consider only the case in which the uniform field is aligned with the x -axis. The normalization factors for both cases are chosen such that the maximum velocity is unity. The initial vortex configurations from (4) and (5) are shown in Fig. 1.

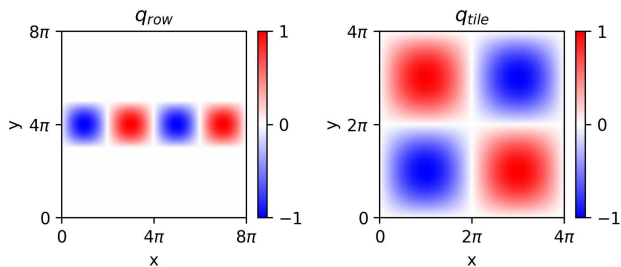


FIG. 1. Initial conditions for the vorticity field, according to (4) (left), and (5) (right).

We thus investigate, numerically, three classes of initial value problems, summarized in Table I. For each of these, we consider a set of four values for the relative strength of the (weak) background magnetic field, namely $M \in \{0, 10^{-3}, 10^{-2}, 10^{-1}\}$. The case $M = 0$ represents the kinematic evolution, in which the magnetic potential A acts as a passive tracer. In all the simulations, we set $Re = Rm = 10^4$; these are both eddy Reynolds numbers, subject to a factor of 2π .

Case	Description
A	q_{row} with $\bar{\mathbf{b}} = \hat{\mathbf{x}}$
B	q_{row} with $\bar{\mathbf{b}} = \hat{\mathbf{y}}$
C	q_{tile} with $\bar{\mathbf{b}} = \hat{\mathbf{x}}$

TABLE I. Table of numerical experiments considered.

III. NUMERICAL METHODS AND DIAGNOSTICS

The numerical library [20] developed for this investigation is written in Python and makes use of the Shenfun computing platform [21, 22], which allows for the simple implementation of the pseudo-spectral method in serial or in parallel using MPI. We evolve the vorticity q and the magnetic potential A in the doubly periodic domain, while the background \bar{A} remains steady in time. For

all simulations, we take $N = 1024$ collocation points in each direction. The solution is evolved in time (with sufficiently small $dt = 2.5 \times 10^{-4}$) through a 3-step Adams-Bashforth (AB3) scheme, where the first step is forward Euler and the second step uses the 2-step Adams-Bashforth method. In all simulations, in order to prevent aliasing errors, we use the exponential-type spectral filter proposed initially by Godon and Shaviv [23]. This filter increases the numerical stability of the code and acts on much smaller scales than the physical diffusion and viscosity.

To quantify the results of the evolution, we consider three quantities for both the kinematic and the magnetic portions of the dynamics as functions of time. First, we consider the Taylor microscale, and its magnetic analogue, defined by

$$L_u = \frac{\langle |\mathbf{u}|^2 \rangle^{1/2}}{\langle q^2 \rangle^{1/2}}, \quad L_b = \frac{\langle |\mathbf{b}|^2 \rangle^{1/2}}{\langle j^2 \rangle^{1/2}}, \quad (6)$$

where angled-brackets indicate a domain average. The lengths L_u and L_b provide estimates of the typical length scales of the turbulent flow and field. An increase (or decrease) in these scales with time tells us whether the kinetic and magnetic energies are moving to larger (or smaller) scales. This allows us to confirm the direction of the energy flux. Next, we consider a bulk measure of the anisotropy of the velocity and magnetic field. Clearly, anisotropy is induced in flows subject to a background magnetic field [24, 25]; furthermore, the choice of initial conditions for the flow may also introduce anisotropy to the system. Specifically, we compute the anisotropy of the velocity $\mathbf{u} = (u, v)$ via

$$\mathcal{A}(\mathbf{u}) = \frac{\langle u^2 \rangle}{\langle u^2 \rangle + \langle v^2 \rangle}, \quad (7)$$

together with the equivalent quantity for the magnetic field, replacing \mathbf{u} by the field $\mathbf{b} = (b_x, b_y)$. These determine, on the range 0 to 1, the induced anisotropy; $\mathcal{A} = 0.5$ corresponds to the isotropic case. Note that initially, $\mathcal{A}(\mathbf{u}) = 0.25$ for flow (4) and $\mathcal{A}(\mathbf{u}) = 0.5$ for flow (5). Finally, we consider the kinetic energy E_K and a scaled version of the magnetic energy \tilde{B}^2 , defined by

$$E_K = \frac{1}{2} \iint |\mathbf{u}|^2 dx dy, \quad \tilde{B}^2 = \frac{\iint |\mathbf{b}|^2 dx dy}{\iint |\bar{\mathbf{b}}|^2 dx dy}. \quad (8)$$

This scaled magnetic energy \tilde{B}^2 is normalized to be unity initially, so as to measure the amplification of the field over time.

IV. SIMULATIONS OF FLUX EXPULSION

In this section, we present numerical results of the dynamical flux expulsion resulting from the three flow and field configurations listed in Table I, using the diagnostic tools described in Section III.

A. Row of Vortices Aligned with the Field

Figure 2 shows snapshots of the vorticity at selected times and for different values of M in the case where a row of vortices with initial vorticity q_{row} , given by expression (4), evolves with a background magnetic field in the x -direction. The first row shows the hydrodynamic (kinematic) limit ($M = 0$, where the field has no effect on the motion), with elliptical vortex cores surrounded by thin filaments of vorticity. Note that the elliptical vortices are created via a hydrodynamic transition from square vortices at early times. The second row shows the vorticity for a very weak dynamical magnetic field ($M = 10^{-3}$). Here the field, although extremely weak, can nonetheless generate small-scale vorticity features that are not present in the kinematic evolution; the field however is not strong enough to disrupt the coherent vortex cores. For $M = 10^{-2}$, shown in the third row, the field, although still very weak on the large scale, is strong enough on the small scale to be dynamically significant: intense, small-scale, vortical structures are generated and ejected into plumes in the y direction. Note the different times for the snapshots in the lower two rows compared with those of the upper two rows. For this particular value of $M = 10^{-2}$, the flow evolves much more quickly than the previous two cases with smaller M ; by the final time shown ($t = 80$), there is little evidence of the original cores. Although the background field is still weak (small M), $M^2 Rm$ is now $O(1)$ and hence, from the scaling argument presented in [7], we might indeed expect the concentrated expelled field to be sufficiently strong to cause vortex disruption. The fourth row of Fig. 2 shows the vorticity for the largest magnetic influence considered here ($M = 10^{-1}$). At this value of M , the field is reasonably strong even on the large scale (although still considerably less than equipartition strength). As such, the vorticity is concentrated into filaments that dominate the flow even at early times ($t = 20$). The flow leads to a complex vorticity distribution, which becomes unstable ($t = 40$), leading to small-scale magnetic turbulence. The resulting evolution is highly oscillatory and shows a pulse in the vorticity traveling in the positive and negative y -directions.

Figure 3 shows snapshots of the total magnetic flux function $\bar{A} + A$ for the same set of simulations as shown in Fig. 2. The two smaller values of M ($M = 0, 10^{-3}$) demonstrate clearly the expulsion of magnetic flux from the centers of the four cores by $t = 200$. With no remaining variation of the flux function within the cores, all field lines (lines of constant $\bar{A} + A$) are therefore expelled from these regions. However, for $M = 10^{-2}$, the large-scale field, although weak, is in the regime where flux expulsion can occur, at least initially, but then the amplified, expelled field is sufficiently strong to disrupt the vortices dynamically. For $M = 10^{-1}$, the large-scale field is sufficiently strong that it is immediately dynamically significant, and hence forestalls the expulsion process. We thus see a qualitative transition of regimes (ex-

hibited by both the vorticity and magnetic flux function) from a hydrodynamic regime to one dominated by the magnetic field. Below, we quantify this transition using various diagnostics.

The left column of Fig. 4 shows the typical length scales of the velocity (top) and magnetic field (bottom), as defined in expressions (6). Note that all diagnostics are plotted up to time $t = 300$. For the kinematic ($M = 0$) case, for which the field exerts no force on the flow, the vortices simply decay on a viscous timescale: L_u is essentially unchanged throughout the evolution. For this kinematic case, magnetic flux is expelled into a thin boundary layer. The scale for the field, L_b , falls sharply from being formally infinite at $t = 0$ (a result of the field being uniform initially) before leveling off once a balance is attained between advection and diffusion; as shown in [1], $L_b = O(Rm^{-1/3})$. For the weak field case of $M = 10^{-3}$, the turbulence induced outside the vortex cores by the interacting vortex filaments leads, at late times, to a slight reduction in L_u , since the flow is no longer totally controlled by the large-scale vortices, and to a slight increase in L_b , since the interaction of the turbulence with the background field leads to magnetic structures on a larger scale than those caused by the flux expulsion process. For the stronger field cases of $M = 10^{-2}$ and $M = 10^{-1}$, there is significant vortex disruption, as discussed above; the flow becomes small scale, resulting in a marked decrease in L_u . For $M = 10^{-2}$, L_b tracks the kinematic evolution only until $t \approx 40$, at which stage vortex disruption sets in; subsequently, the magnetic field is no longer exclusively small scale and so L_b grows, greatly exceeding its kinematic value. For $M = 10^{-1}$, the initial decline in L_b is halted even before the saturated kinematic level is attained; the field is then large scale (as measured by L_b) throughout the evolution.

The middle column of Fig. 4 shows the evolution of the kinetic energy E_k and the magnetic field amplification \bar{B}^2 . For the kinematic evolution, E_k is essentially constant over the time interval shown: the very slow decay on a viscous timescale is not discernible. The magnetic field is amplified to a peak energy (B_1^2 in the notation of [1]), before saturating at a lower level (B_2^2). In our simulations, over times much longer than shown in Fig. 4 — and in contrast to [1], where the flow is prescribed — the vorticity will eventually decay and the field will revert to its initial uniform state. The kinematic scalings of [1] suggest that B_1^2 and B_2^2 should scale as $Rm^{2/3}$ and $Rm^{1/2}$, respectively. However, since we do not investigate multiple values of Rm , we cannot determine the proportionality constant to see if our results align with these scalings. For $M = 10^{-3}$, the turbulence induced at a late stage leads to enhanced dissipation of both kinetic and magnetic energies in comparison with the case of $M = 0$. For $M = 10^{-2}$, the magnetic field amplification initially follows the kinematic time trace, but ends abruptly once dynamical effects become important. The subsequent vortex disruption then leads to dissipation of the magnetic energy. It is of interest to note that

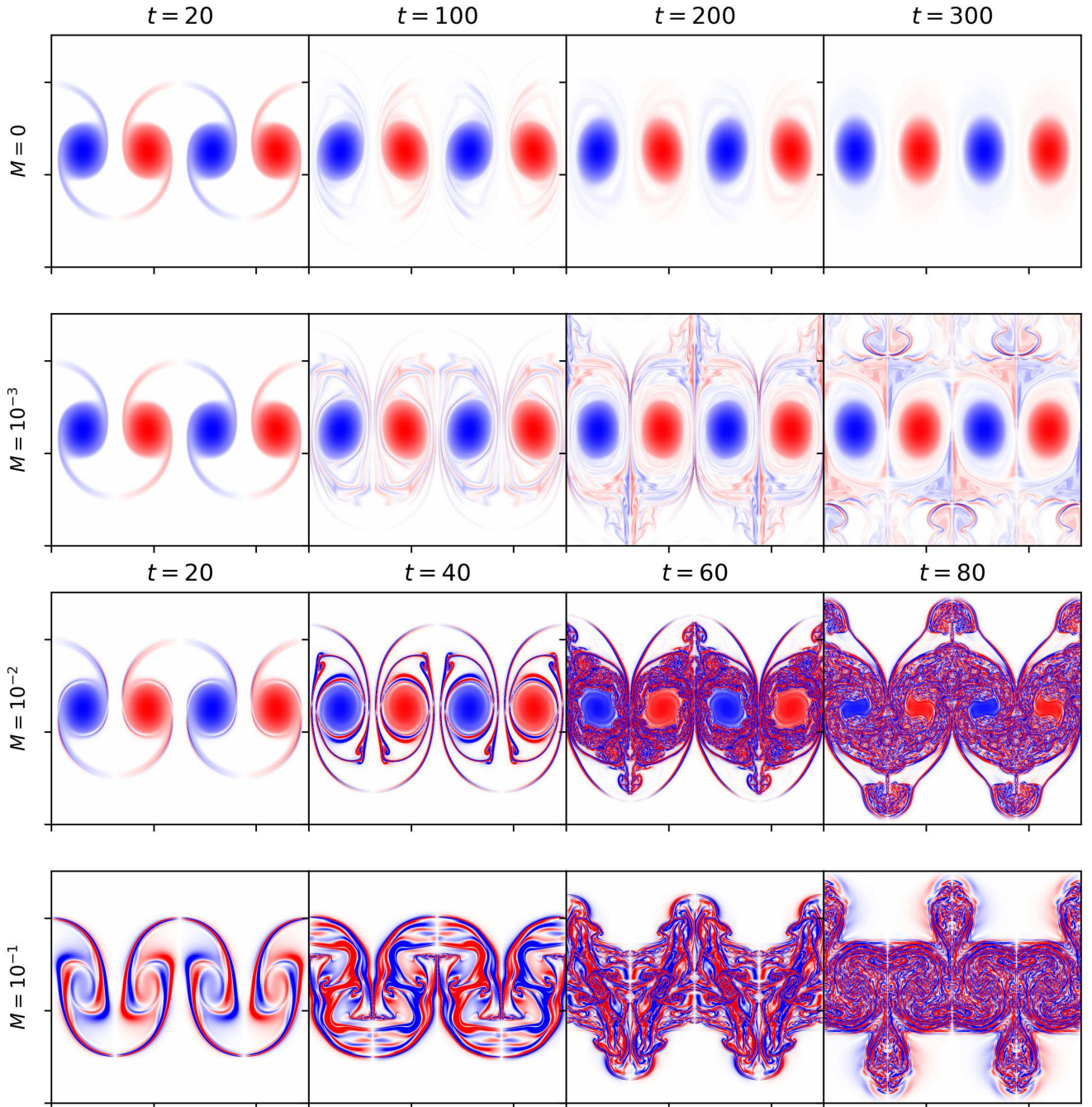


FIG. 2. Snapshots of the vorticity q for increasing $M = 0, 10^{-3}, 10^{-2}, 10^{-1}$, at times $t = 20, 100, 200, 300$ for the two smallest values of M , and at times $t = 20, 40, 60, 80$ for the two largest. The initial condition has $q = q_{rov}$ with a background magnetic field $\vec{b} = \hat{x}$ (case A).

the departure from the kinematic evolution occurs at an earlier time for E_k than for \tilde{B}^2 . Some small-scale turbulence is generated even while the field is still being amplified; this leads to a reduction in E_k by a factor of about ten in $50 \lesssim t \lesssim 100$. For the strongest field case considered, with $M = 10^{-1}$, the background field is sufficiently strong that its dynamical influence is such that there is very little amplification of magnetic energy. The Lorentz force induces oscillations in the flow, leading to an increase in E_k after an initial decrease. As shown in Fig. 2, hydrodynamic instabilities lead rapidly to small-scale turbulence and thus (oscillatory) decay of E_k .

The right column of Fig. 4 shows the anisotropy measures of the velocity (top) and magnetic field (bottom), as defined by Eq. (7). Initially, $\mathcal{A}(\mathbf{u}) = 0.25$ and $\mathcal{A}(\mathbf{b}) = 1$, reflecting the anisotropy of the flow and that of the unidirectional imposed field. For $M = 0$ and $M = 10^{-3}$, $\langle v^2 \rangle$ is the dominant contribution to the kinetic energy throughout. However, for $M = 10^{-2}$ and $M = 10^{-1}$, the kinetic energy at long times is distributed isotropically, at least on average. It is therefore of interest to examine the vorticity at long times. Figure 5 shows the long-time behavior of the vorticity for the case of $M = 10^{-2}$ — at much longer times than shown in Fig. 2. In comparison with the first and second rows of Fig. 2 ($M = 0, 10^{-3}$), in which the vortex cores are still visible even at long times, here there is no trace of the original cores at long times; the vorticity field is rather turbulent. For $M = 10^{-1}$, the stronger field leads to oscillatory behavior, reflected in $\mathcal{A}(\mathbf{u})$. For all four values of M , the anisotropy measure of the magnetic field $\mathcal{A}(\mathbf{b})$ initially declines rapidly, reflecting the generation of (strong) field in the y -direction from a (weak) field initially in the x -direction. For the kinematic evolution, $\mathcal{A}(\mathbf{b})$ continues to decrease, with a long-time value of $\mathcal{A}(\mathbf{b}) \approx 0.1$. For the case of $M = 10^{-3}$, $\mathcal{A}(\mathbf{b})$ tracks the kinematic evolution until at late times there is a deviation from kinematic behavior, again with an almost isotropic distribution of magnetic energy. For $M = 10^{-2}, 10^{-1}$, the decrease in $\mathcal{A}(\mathbf{b})$ is quickly halted once the field becomes dynamically effective, leading to a roughly isotropic distribution of magnetic energy.

From the four values of M we have investigated, we have been able to identify four distinct regimes. For $M = 0$ (the kinematic regime, in which the field is decoupled from the flow), classical flux expulsion occurs, as described in [1]. For $M = 10^{-3}$, the evolution is essentially kinematic, although even this extremely weak field has some dynamical influence at long times. For $M = 10^{-2}$, $M^2 Rm$ becomes $O(1)$, and hence is in the vortex disruption regime identified by [7]. Here, flux is initially expelled, but becomes of sufficient strength to disrupt the expelling vortex. For $M = 10^{-1}$, the field is sufficiently strong, even on the large scales, that there is little, if any, flux expulsion. Wave-like motions are induced by the Lorentz force, again leading, by a different mechanism, to total vortex disruption.

B. Row of Vortices Perpendicular to the Field

In this subsection, we again present results for simulations with initial vorticity q_{row} , but now with the background magnetic field in the y -direction. Figure 6 shows snapshots of the vorticity at the same times and for the same values of M as in Fig. 2. Differences between the first two rows of Fig. 6 can be identified only on very close inspection. Thus the case of $M = 10^{-3}$ here is essentially kinematic, in contrast to the case where the imposed field is in the x -direction, for which small-scale dynamically-driven vortical features can be seen in the second row of Fig. 2. When $M = 10^{-2}$, there is evidence of vortex disruption, but it is noteworthy that the vortices are much more coherent, at the equivalent field strength and time, than with a background field in the x -direction (third row of Fig. 2). For the strongest imposed field case of $M = 10^{-1}$, filaments of vorticity are elongated in the y -direction, with strong oscillations in the long-time evolution; the contrast with Fig. 2 is again marked. Clearly, for all values of the imposed field strength, the orientation of the background field with respect to the row of vortices is critical to how the vortices evolve.

The magnetic flux function in the top two rows of Fig. 7 ($M = 0, 10^{-3}$) exhibits classical kinematic flux expulsion; by the final time shown, there is very little variation remaining in the vortex cores. For $M = 10^{-2}$ (third row), at $t = 80$ the flux function still shows the spiral structure arising from winding up the magnetic field; at this time, the evolution is still not significantly different from the kinematic case. It is noteworthy that the evolution of the flux function is much more ordered than for the equivalent field strength in case A — contrast the $t = 80$ plots in Fig. 3 and Fig. 7. For $M = 10^{-1}$ (fourth row), flux expulsion is soon halted as a result of the stronger background field. For the time interval shown, the dominant feature is the elongation in the y -direction, fluid motion being less constrained in the direction of the imposed field. We note again how different the evolution is to that of case A, where the background field is aligned with the row of vortices.

The diagnostics in Fig. 8 shed further light on the behavior exhibited in Fig. 6 and Fig. 7. The first thing to note is that the kinematic diagnostics are similar to those of case A, except for the energy amplification \tilde{B}^2 , which is markedly different. Whereas for an imposed field parallel to the row of vortices (case A) there is energy amplification of nearly 800, here, for an imposed perpendicular field, the amplification is ten times smaller. What is also immediately noticeable is that — in contrast to case A — the kinematic ($M = 0$) and weakest dynamical field ($M = 10^{-3}$) cases are indistinguishable throughout the evolution shown, for all the diagnostic measures. For $M = 10^{-2}$, as in case A, the departures from the kinematic evolution for flow and magnetic field diagnostics occur at different times. The length L_u starts to decrease at $t \approx 50$, as small-scale motions are generated. However, L_b follows the kinematic trace until $t \approx 200$; as

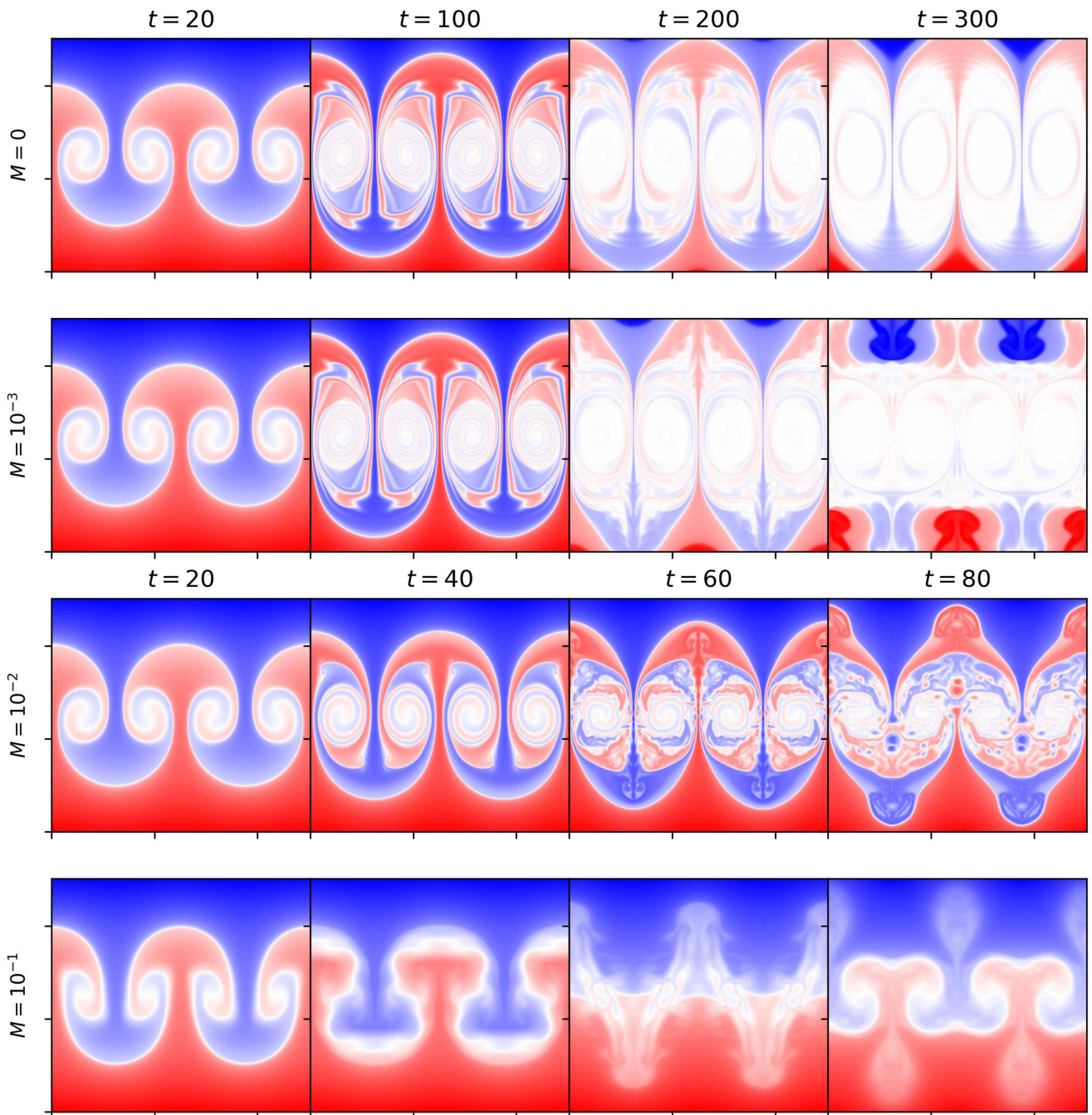


FIG. 3. Snapshots of the magnetic flux function ($\bar{A} + A$) for increasing $M = 0, 10^{-3}, 10^{-2}, 10^{-1}$, at times $t = 20, 100, 200, 300$ for the two smallest values of M , and at times $t = 20, 40, 60, 80$ for the two largest, for case A.

in case A, despite the velocity field being changed from its initial state, flux expulsion is still the dominant mechanism regarding the magnetic field, up to this later time. For $t \gtrsim 200$, there is clearly a change in the dynamics, as illustrated by L_b , \tilde{B}^2 , $\mathcal{A}(\mathbf{u})$ and $\mathcal{A}(\mathbf{b})$. Figure 9 shows the vorticity snapshots for the case of $M = 10^{-2}$ at longer times. The original vortex cores survive, to some extent, until $t \approx 200$, but are then destroyed by the surrounding small-scale turbulence. The turbulence then fills the domain, leading to roughly isotropic measures of flow and field. The enhanced turbulence at $t \approx 200$ acts on the relatively ordered flux-expelled magnetic field, leading to an initial amplification in magnetic energy (\tilde{B}^2). The dominant scale for the field is no longer the boundary layer scale of the expelled field, and so L_b increases, despite the increase in \tilde{B}^2 . At the final time shown, both the flow and field are roughly isotropic. For $M = 10^{-1}$, the background field is again of sufficient strength to influence the dynamics throughout. The small kinematic value for L_b is never attained, and amplification of magnetic energy is relatively small in comparison with the weaker fields considered. As in case A, the stronger background field induces wave-like motions, whose effects can be seen, for example, in the oscillations in L_u and L_b . However, in contrast to case A, the flow and field remain anisotropic throughout, with the preferred (y) direction being that of the imposed field.

As in case A (imposed field aligned with the row of vortices), as the imposed field strength is increased, we can identify regimes of kinematic behavior, of vortex disruption, and of magnetically-dominated dynamics. There are, however, some important differences. For the perpendicular field case, a stronger background field is required before any dynamical influence is observed. In a similar manner, for $M = 10^{-2}$, vortex disruption does not occur immediately after flux has been expelled, as in [7] and case A. Instead, small-scale turbulence is generated outside the vortex cores, as shown in Fig. 9, and it is this turbulence that is responsible for the late-time destruction of the vortex cores. For the strongest background field considered ($M = 10^{-1}$), the geometry of the field is such as to maintain anisotropy throughout the evolution.

C. Two by Two Vortices

Finally we investigate the case of a two by two tile of vortices with initial vorticity q_{tile} , given by (5). The evolution of the vorticity is depicted in Fig. 10. In contrast to the hydrodynamic ($M = 0$) evolution starting from an initial condition of $q = q_{row}$, here there is no change of form of the vortices; the hydrodynamic evolution (top row of Fig. 10) is identically satisfied by $q = \exp(-t/2Re)q_{tile}$. However, even with a very weak background field ($M = 10^{-3}$), as shown in the second row of Fig. 10, there is clear evidence of the dynamical influence of the Lorentz force. By $t = 20$, a sheath

of opposite-signed vorticity has formed around each vortex core. These sheaths subsequently grow in width (e.g. $t = 100$) and eventually become unstable, with the vortex cores surrounded by turbulent vortex filaments (as seen at $t = 200$). Note though that by the final time shown ($t = 300$), there is no wholesale destabilization of the vortex cores. With $M = 10^{-2}$, the vorticity filaments grow rapidly, as can be seen in the plot at $t = 20$. These interact to give rise to smaller vortices through a secondary instability ($t = 40$). The flow has two distinct spatial phases, with reasonably laminar vortex cores living in a turbulent vortex sea. At longer times, the vortex cores are gradually eroded by the surrounding turbulence. For the case of the strongest field considered ($M = 10^{-1}$), thick bands of vorticity appear that wind and unwind in place of the original vortex cores, generating smaller-scale features and a complex turbulent flow thereafter.

Figure 11 shows the corresponding evolution of the magnetic flux function. As expected, the kinematic evolution shows the expulsion of magnetic field to the periphery of the large-scale vortices. It is though noticeable that at $t = 300$, and in contrast to cases A and B, some remnant of the field remains at the centers of the core. Whereas flux can be expelled in a relatively unconstrained manner from the row of vortices, the more constrained geometry of the two by two periodic tile leads to competition in the expulsion process between the various vortices, leading to a longer period for full expulsion to occur. For $M = 10^{-3}$, the initial evolution of the magnetic flux (certainly up to $t = 100$) is essentially indistinguishable from the kinematic case. However, at later times, the effects of the interaction of the vortex filaments (seen in Fig. 10) with the magnetic field is clearly seen at the edge of the cells. As for cases A and B, the dynamical effects of the field are felt fully by $M = 10^{-2}$. As seen in Fig. 10, the Lorentz force drives a strong sheath of counter-vorticity around the vortex cores. By $t = 40$, the sheath and the field have become disrupted, with the flux having been expelled from the vortex cores. For $M = 10^{-1}$, the background field is again strong enough to be dynamically significant, retaining a large-scale component, despite the small-scale vorticity observed in Fig. 10.

The kinematic evolution of L_b , shown in Fig. 12, is very similar to that for cases A and B. The amplification of magnetic energy is greater than for case B but less than that of case A. The anisotropy measure $\mathcal{A}(\mathbf{b})$ initially decreases from its starting value of unity but, unlike in case A, increases again, with $\mathcal{A}(\mathbf{b}) \approx 0.9$ at later times; this final value reflects the anisotropy of the background field, the flow being isotropic. For $M = 10^{-3}$, the diagnostic measures follow those of the kinematic case until $t \approx 150$. At this point, the disruption of the vortex sheaths leads to a pronounced growth in magnetic energy and to the field becoming, on average, isotropic. We note though that the overall length scale of the field, L_b , is similar to that when $M = 0$. As in cases A and B, the diagnostics for the two strongest field cases ($M = 10^{-2}$ and $M = 10^{-1}$) have certain characteris-

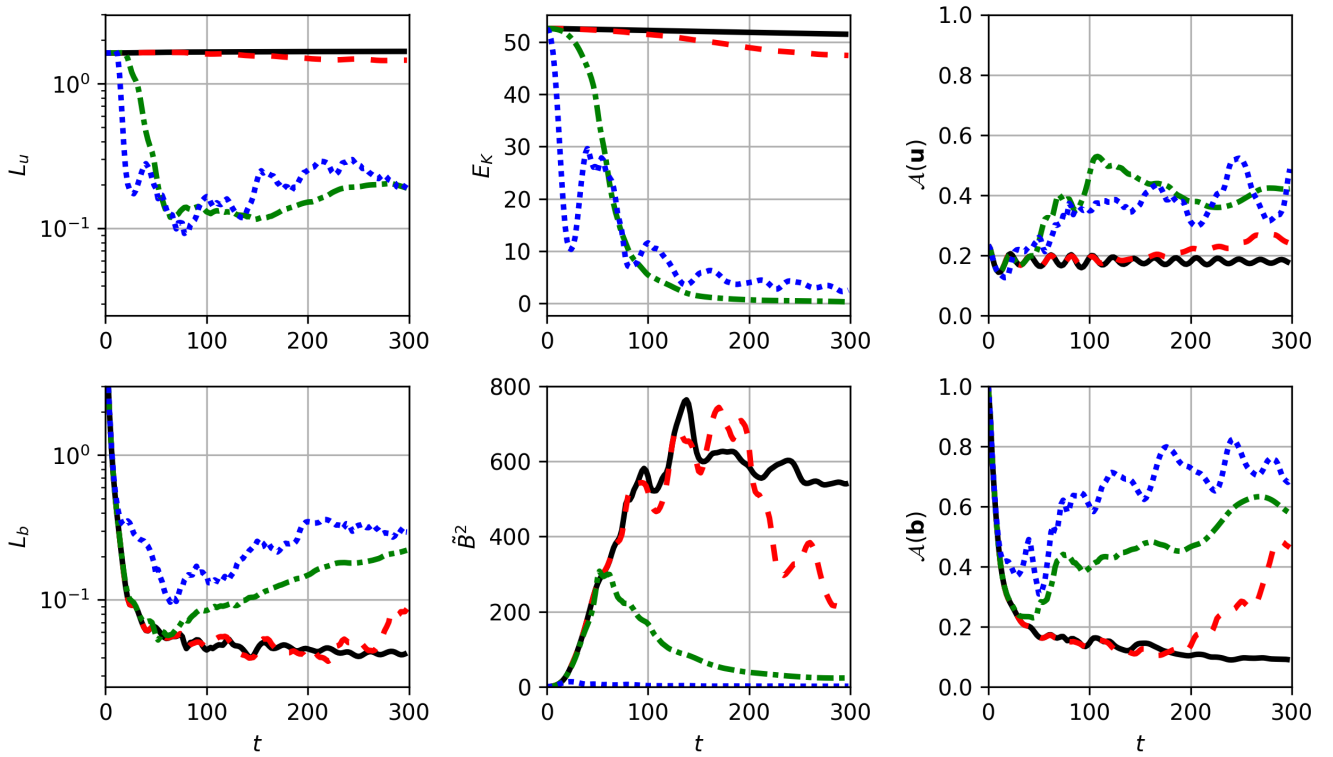


FIG. 4. Field and flow diagnostics as a function of time for case A. The four different values of M are shown as: $M = 0$ (solid black), 10^{-3} (dashed red), 10^{-2} (dot-dashed green) and 10^{-1} (dotted blue). Left column: microscales for the velocity (L_u , top) and magnetic field (L_b , bottom), defined in (6). For reference, the lower plotting limit of the y -axis is chosen as the grid scale ($L/N = 8\pi/1024$). Middle column: total kinetic energy (E_K , top) and total scaled magnetic energy (\tilde{B}^2 , bottom). Right column: anisotropy norms for the velocity ($\mathcal{A}(\mathbf{u})$, top) and magnetic field ($\mathcal{A}(\mathbf{b})$, bottom), defined in (7).

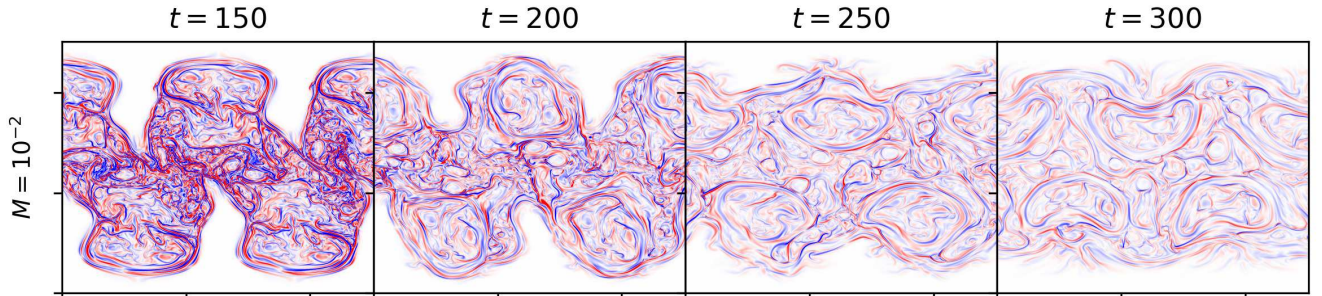


FIG. 5. Vorticity snapshots of case A for $M = 10^{-2}$, as in the third row of figure 2, but at longer times. This case corresponds to the green curves of Fig. 4 and shows how the velocity field approaches near isotropy, as measured by $\mathcal{A}(\mathbf{u})$.

tics in common, and considerable differences from the weaker field cases. Here there is essentially no period of kinematic evolution: small velocity scales are generated at very early times (leading to a decrease in L_u), while the background field is of sufficient strength that full flux expulsion, leading to a small value of L_b , is not attained. Instead, as the field becomes disordered, there is an increase in the magnetic microscale L_b . The rapid fall-off in kinetic energy is similar to that of case A, shown in Fig. 4. For $M = 10^{-2}$, the velocity remains essentially isotropic throughout, and the long-time magnetic field is also roughly isotropic ($\mathcal{A}(\mathbf{b}) \approx 0.6$). By contrast, for $M = 10^{-1}$, for which there is little amplification of the magnetic energy, the background field is sufficiently strong that the long-term state has high degrees of anisotropy in both the field and flow. This can be seen in Fig. 13, which shows the evolution of the vorticity for $t > 150$. The increasing anisotropy in time is apparent. It is though worth pointing out, as can be seen from the plot of E_k in Fig. 12, that the kinetic energy of the flows shown in Fig. 13 is extremely small in comparison with the initial energy of the two by two vortices: most of the energy has been dissipated viscously through the small scales generated.

V. DISCUSSION

In this paper we have investigated the evolution of an initially uniform magnetic field in vortical flows at high Rm (i.e., high electrical conductivity). While the fundamental mechanism of flux expulsion is inherently kinematic, as first illustrated by Weiss [1], we have extended the problem into the dynamical regime by considering the back-reaction of the field on the flow. We have investigated various arrangements of vortices in a relatively simple two-dimensional incompressible MHD model. While much more complex models exist to study flows in astrophysics, process studies such as this allow us to understand the underlying dynamics in an approachable way. We have considered a row of vortices either aligned (case A) or orthogonal (case B) to the initial field, together with a tile of two by two vortices (case C). For each of the three different configurations, we considered background magnetic fields of four different strengths in order to assess the impact of the field on the overall dynamics. In so doing, we identified four different dynamical regimes.

When $M = 0$, the evolution is kinematic (the field has no influence on the flow); as expected, all three configurations exhibit classical flux expulsion, in which magnetic field lines are expelled to the edges of the vortex cores. When M is non-zero but very small (such that even M^2Rm is still small), the Lorentz force can nonetheless induce small-scale features in the vorticity but is not strong enough to disrupt the vortex cores and their expulsion of magnetic flux. For $M^2Rm = O(1)$, the inwards Lorentz force resulting from the expelled flux can be suffi-

ciently strong to disrupt both the shape and extent of the vortex cores; this is the vortex disruption regime identified in [7]. For $M^2 \lesssim O(1)$, but with $M^2Rm \gg 1$, the background field is sufficiently strong to influence the evolution throughout.

While the kinematic regime has been widely studied, and the vortex disruption regime to some extent, our study has shed light on two other regimes. The first lies between the kinematic and disruptive regimes, where the field can generate small-scale structures in the flow, but cannot disrupt large-scale coherent vortices. The second is beyond the vortex disruption regime, but where the initial magnetic energy is still smaller than the kinetic energy of the flow. Coherent vortices are almost immediately destroyed from an initial uniform field that is strong enough to be dynamically active. The resulting flow is oscillatory, as vortices attempt to wind-up magnetic field lines, and fight against magnetic tension, preventing their deformation.

There are a number of common features between the various configurations studied, but also some differences that are worth noting. In the kinematic regime, L_b tends to roughly the same value for all three configurations — as expected, since this scale is determined by Rm . It can be seen that the anisotropy of the field, measured by $\mathcal{A}(\mathbf{b})$, is essentially the same for cases A and B; thus, despite the different orientations of the background field, $\mathcal{A}(\mathbf{b})$ is here primarily determined by the anisotropy of the flow. For case C, for which the flow is isotropic, the long-term value of $\mathcal{A}(\mathbf{b})$ must result from the orientation of the background field. The kinematic amplification of the field in case A is markedly greater than that for case B. The flow configuration in case C also suggests that flux expulsion is somewhat impeded when a vortex core is completely surrounded by others, each attempting to expel their own magnetic flux. For $M = 10^{-3}$, the evolution in case B is essentially kinematic throughout. By contrast, even this extremely weak background field has late-time dynamical consequences in cases A and C, most clearly manifested through $\mathcal{A}(\mathbf{b})$. For $M = 10^{-2}$ — the vortex disruption regime — the initial tendency to flux expulsion, marked by a decrease in L_b , is halted abruptly for all three configurations. The dynamical effects of the field are thus reflected in a subsequent increase in L_b and a decrease in L_u as a consequence of the small-scale flows generated. The small-scale turbulence provides a very efficient mechanism for the dissipation of kinetic energy, though this is less marked for case B. For $M = 10^{-2}$, the long-term states for all configurations are essentially isotropic in both flow and field. For $M = 10^{-1}$, for all configurations, the background field is sufficiently strong that the kinematic level of L_b is never attained; the microscale for the field always greatly exceeds the kinematic value. Furthermore, field amplification for all configurations is very small compared with that for the smaller values of M . The relatively strong background field leads to oscillations induced by the Lorentz force, which can be seen, for example, in $\mathcal{A}(\mathbf{u})$. It is of interest to note that

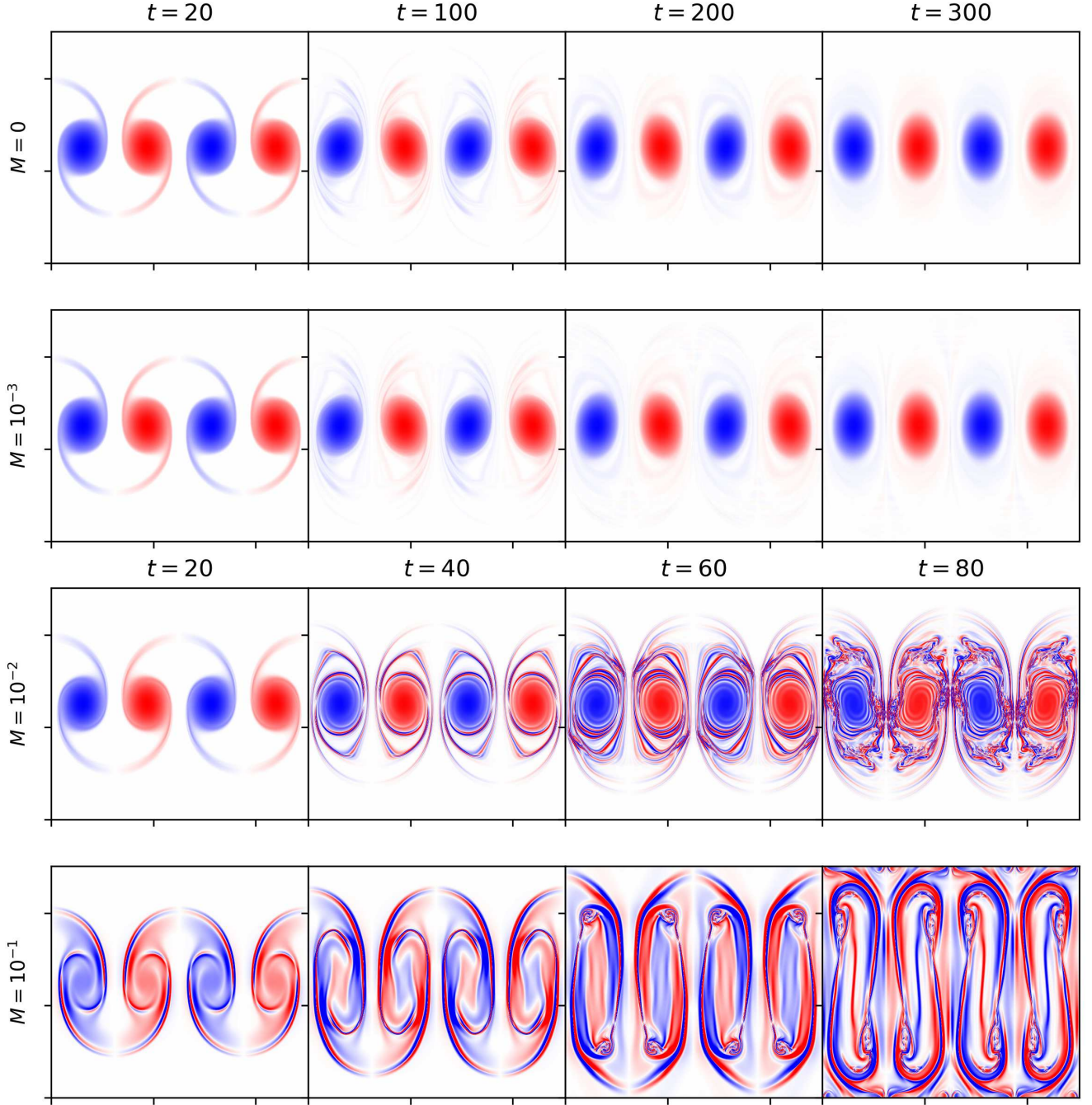


FIG. 6. Snapshots of the vorticity q for increasing $M = 0, 10^{-3}, 10^{-2}, 10^{-1}$, at times $t = 20, 100, 200, 300$ for the two smallest values of M , and at times $t = 20, 40, 60, 80$ for the two largest. The initial condition has $q = q_{rov}$ with a background magnetic field $\bar{\mathbf{b}} = \hat{\mathbf{y}}$ (case B).

whereas the evolution of cases A and C (with $M = 10^{-1}$) lead rapidly to a highly turbulent flow, that of case B (field orthogonal to row of vortices) produces much more laminar elongated vortices.

The differences between the three considered geometries lie in the degree of symmetry of the vortex arrangement and, for two cases, the relative orientation of the vortex array and the imposed field. In cases A and B, the vorticity array is anisotropic, with q_{row} concentrated along a single band spanning a quarter of the y -domain. Consequently, the relative orientation of the field to this band dictates the features that arise in the nonlinear evolution. For case A (imposed field parallel to row of vortices), field lines in the center of the domain run across — and are therefore deformed by — all four vortices. The counter-rotating vortices induce a strong Lorenz force in the highly distorted field, and consequent vortex disruption. By contrast, any field line from case B (imposed field perpendicular to row of vortices) passes through at most one vortex. Field line distortion and, consequently, vortex disruption are reduced in comparison to case A. The differences between cases A and B are particularly stark for the strongest considered field. For case A, the induced Lorenz force leads to complete vortex disruption and to a turbulent flow; for case B, however, the vortices remain essentially laminar, and are stretched out along the field lines as magnetic tension opposes any attempt at distortion. The key difference of case C (for which the vortices form the periodic array q_{tile}) is that the vortex distribution is isotropic. Although field lines are heavily distorted, as in case A, disruption is somewhat inhibited, since each vortex is constrained to some extent by its four neighbors of opposing polarity.

In all of our simulations, we have set $Re = Rm \gg 1$; i.e., magnetic Prandtl number $Pm = \nu/\eta = 1$. Astrophysically, Re and Rm are typically both large, but their ratio Pm can be large, $O(1)$ or small, depending on context. In galaxies, $Pm \gg 1$; in the solar interior, Pm is less than unity, but not particularly small ($O(10^{-1})$ in the tachocline); in the interiors of the giant planets, $Pm \ll 1$. It is important, therefore, to consider the possible consequences of variations in Pm . For the kinematic problem, Re plays very little role; the flow is prescribed initially and decays slowly on a viscous time scale; the flow remains as a large-scale eddy. However, once the field is dynamically significant and small-scale vorticity is generated, then the role of Pm may well be significant. In our simulations, with $Pm = 1$, the small-scale field and small-scale vorticity are on an equal footing. We envisage that the evolution for $Pm > 1$ will be broadly similar, with less intense vortex interactions. More significant changes in the evolution are expected when $P \ll 1$, owing to the more concentrated vorticity. However, a computational study of the regime $Re \gg Rm \gg 1$ is currently unobtainable; with both $Re \gg 1$ and $Rm \gg 1$, it is unavoidable that Pm cannot be too large or too small.

From an astrophysical perspective, our study has pro-

vided a further example of how a very weak large-scale magnetic field (M^2 small) can nonetheless become dynamically significant on small scales, provided Rm is sufficiently large. Indeed, we have not only given illustrations of vortex disruption when $M^2 Rm = O(1)$, but have shown how the vortex dynamics can be somewhat influenced even for $M^2 Rm \ll 1$. It is thus of interest to consider the implications of these findings for different types of astrophysical body.

In the Sun, Rm is large, although, dependent on context, there is quite a range for its estimated value. Based on the (slow) radial flows across the tachocline, Rm may be as low as a few hundred [26]. Conversely, much higher estimates of 10^9 can be derived for the deep convection zone or 10^6 for the photosphere [27]. Our work has addressed the interaction of vortical flows with a background magnetic field, and so possibly the most relevant solar application would be to models such as [28], which seek to explain the confinement of the tachocline through essentially hydrodynamic meridional flows, with a thin magnetic boundary layer separating the field in the radiative interior from the field-free region above. The proposed flows are very slow ($\sim 10^{-5} \text{ cm s}^{-1}$), thus giving $Rm \sim 10^3$ for a length scale based on the tachocline width. On taking $\rho = 0.2 \text{ g cm}^{-3}$ [29], the condition $M^2 Rm = O(1)$ translates into a critical field strength of the order of $5 \times 10^{-7} G$. Thus an incredibly weak magnetic field could have a dynamical effect on the flow structure proposed, suggesting that purely hydrodynamical considerations may be unrealistic. It should also be mentioned that other objections have been advanced to the idea of an entirely field free region in the tachocline (see, e.g., [30]). In the convection zone itself, the motions arise from highly supercritical turbulent convection; although there will undoubtedly be some sort of flux expulsion, the turbulent dynamics renders the physics very different to that investigated here.

A notable characteristic of the gas giants is that the electrical conductivity σ falls precipitously with radius towards the surface of the planets. The ab initio simulations of [31] suggest that σ in Jupiter declines by about twelve orders of magnitude over the outer 10% by radius. Similar calculations for Saturn [32] suggest a similar (though slightly less dramatic) story, with a decline in σ of ten orders of magnitude over the outer 30% by radius. The vast range in σ leads to a similarly large range in Rm . For example, on adopting a typical zonal wind strength on Jupiter of 100 ms^{-1} , and a length scale of one tenth of the planetary radius R_J , Rm varies from $O(10^{-3})$ at the surface to $O(10^9)$ in the deeper interior. The interior magnetic fields of Jupiter and Saturn are the result of turbulent dynamo action at high Rm [33], and, as in the solar context, our models of flux expulsion are not immediately applicable in such dynamo regions. However, in the surface regions, the idea of vortical flows in the presence of a weak background magnetic field is of immediate relevance. The strength of the dipolar field at the Jovian surface is $O(10G)$. Adopting

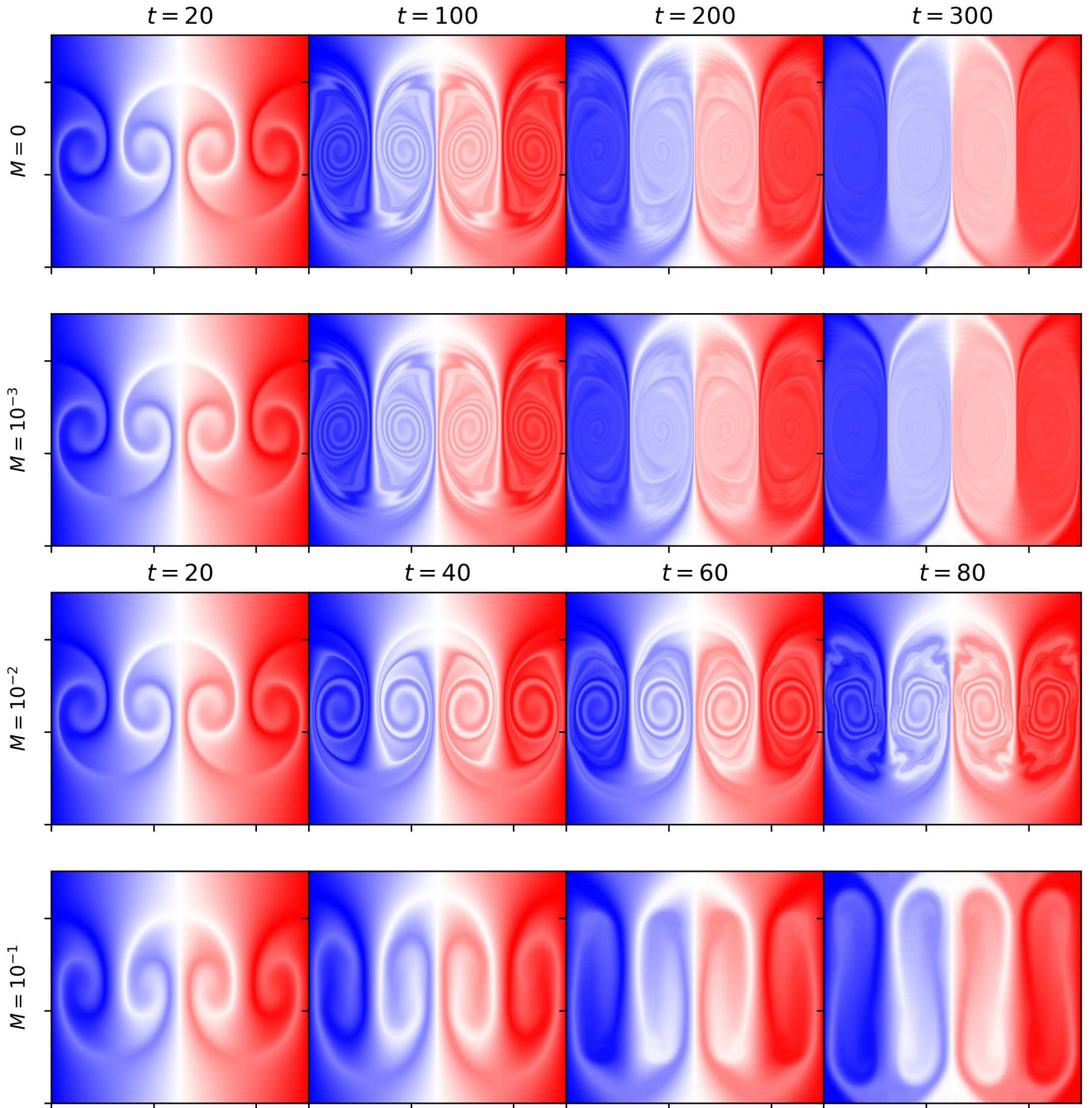


FIG. 7. Snapshots of the magnetic flux function ($\bar{A} + A$) for increasing $M = 0, 10^{-3}, 10^{-2}, 10^{-1}$, at times $t = 20, 100, 200, 300$ for the two smallest values of M , and at times $t = 20, 40, 60, 80$ for the two largest, for case B.

a characteristic flow speed of 100 ms^{-1} and a representative density of $\rho = 0.1 \text{ g cm}^{-3}$ [31] provides the estimate $M^2 = O(10^{-6})$. The condition $M^2 Rm = O(1)$ is then satisfied at roughly $r = 0.95 R_J$ [31], suggesting that magnetohydrodynamical effects will certainly come into play by this depth. Although the scaling argument is of course not particularly precise, it does highlight the important feature that a hydrodynamic description will be valid only for the upper surface layers and that the influence of the magnetic field will be felt at radii somewhat greater than where the conductivity reaches its full interior value. Indeed, it is of interest to note that the estimate $r = 0.95 R_J$ is consistent with the depth of the surface zonal flows inferred from recent Juno measurements [34]. We envisage that a similar argument holds for Saturn, although the weaker surface field strength and the less steep variation of electrical conductivity means that the transition between hydrodynamical and magnetohydrodynamical behavior would lie at a smaller radius.

Here we have concentrated on the simplest case of two-dimensional fields and flows, for which the interactions between the vorticity and magnetic fields are most pronounced and most readily understood. It would certainly therefore be of interest to extend the studies to a three-dimensional geometry. The most natural way of doing

this is to consider stratified systems that favor quasi-two-dimensional behavior. A study of decaying vortices in the shallow-water MHD system would complement the investigation [7] of the formation and possible disruption of vortices arising via instabilities of shear layers and jets. A related system is that of quasi-geostrophic shallow-water MHD [35], which extends the two-dimensional dynamics to include the competition between the influences of stratification and rotation (measured by, for example, the Burger number), as well as incorporating beta-plane dynamics. Some interesting progress has already been made along these lines ([36], [37]).

ACKNOWLEDGMENTS

JT would like to acknowledge the support of his NSERC CGS-M graduate scholarship. FJP would like to acknowledge financial support of his NSERC Discovery Grant. DWH would like to thank the Isaac Newton Institute for Mathematical Sciences, Cambridge, for support and hospitality during the programme Anti-diffusive dynamics: from sub-cellular to astrophysical scales, where work on this paper was undertaken. The programme at the Isaac Newton Institute was supported by EPSRC grant EP/R014604/1.

-
- [1] N. O. Weiss, The expulsion of magnetic flux by eddies, *Proc. R. Soc. Lond. A* **293**, 310 (1966).
 - [2] J. H. Thomas and N. O. Weiss, Fine structure in sunspots, *Annu. Rev. Astron. Astrophys.* **42**, 517 (2004).
 - [3] J. Bloxham, The expulsion of magnetic flux from the Earth's core., *Geophys. J. R. Astron. Soc.* **87**, 669 (1986).
 - [4] N. O. Weiss and M. R. E. Proctor, *Magnetoconvection* (Cambridge University Press, 2014).
 - [5] H. K. Moffatt and H. Kamkar, On the time-scale associated with flux expulsion, in *Stellar and Planetary Magnetism*, edited by A. M. Soward (Gordon and Breach, 1983).
 - [6] P. B. Rhines and W. R. Young, How rapidly is a passive scalar mixed within closed streamlines?, *J. Fluid Mech.* **133**, 133 (1983).
 - [7] J. Mak, S. D. Griffiths, and D. W. Hughes, Vortex disruption by magnetohydrodynamic feedback, *Phys. Rev. Fluids* **2**, 113701 (2017).
 - [8] J. Mak, *Shear Instabilities in Shallow-Water Magnetohydrodynamics*, Ph.D. thesis, University of Leeds (2013).
 - [9] A. D. Gilbert, J. Mason, and S. M. Tobias, Flux expulsion with dynamics, *J. Fluid Mech.* **791**, 568 (2016).
 - [10] F. Cattaneo and S. I. Vainshtein, Suppression of turbulent transport by a weak magnetic field, *Astrophys. J.* **376**, L21 (1991).
 - [11] R. M. Kulsrud and S. W. Anderson, The spectrum of random magnetic fields in the mean field dynamo theory of the galactic magnetic field, *Astrophys. J.* **396**, 606 (1992).
 - [12] L. Tao, F. Cattaneo, and S. I. Vainshtein, Evidence for the suppression of the alpha-effect by weak magnetic fields., in *Solar and Planetary Dynamos*, edited by M. R. E. Proctor, P. C. Matthews, and A. M. Rucklidge (Cambridge University Press, 1993) pp. 303–310.
 - [13] A. V. Gruzinov and P. H. Diamond, Self-consistent theory of mean-field electrodynamics, *Phys. Rev. Lett.* **72**, 1651 (1994).
 - [14] F. Cattaneo and D. W. Hughes, Nonlinear saturation of the turbulent α effect, *Phys. Rev. E* **54**, 4532 (1996).
 - [15] S. R. Keating, L. J. Silvers, and P. H. Diamond, On cross-phase and the quenching of the turbulent diffusion of magnetic fields in two dimensions, *Astrophys. J.* **678**, L137 (2008).
 - [16] T. Kondić, D. W. Hughes, and S. M. Tobias, The decay of a weak large-scale magnetic field in two-dimensional turbulence, *Astrophys. J.* **823**, 111 (2016).
 - [17] S. M. Tobias, P. H. Diamond, and D. W. Hughes, β -plane magnetohydrodynamic turbulence in the solar tachocline, *Astrophys. J. Lett.* **667**, L113 (2007).
 - [18] C. Guervilly, D. W. Hughes, and C. A. Jones, Generation of magnetic fields by large-scale vortices in rotating convection, *Phys. Rev. E* **91**, 041001 (2015).
 - [19] Ramirez, F. R. and Diamond, P. H., Evolution of layered patterns of active scalar fields (2023), preprint on webpage at <https://www.newton.ac.uk/event/adi/>.
 - [20] J. Tessier and F. Poulin, Quasi-Geostrophic Magnetohydrodynamics - (Python code, powered by Shenfun), <https://github.com/jonathan-tessier/qgmhd> (2022).
 - [21] M. Mortensen, Shenfun: High performance spectral Galerkin computing platform, *J. Open Source Softw.* **3**, 1071 (2018).
 - [22] M. Mortensen, Shenfun — automating the spectral

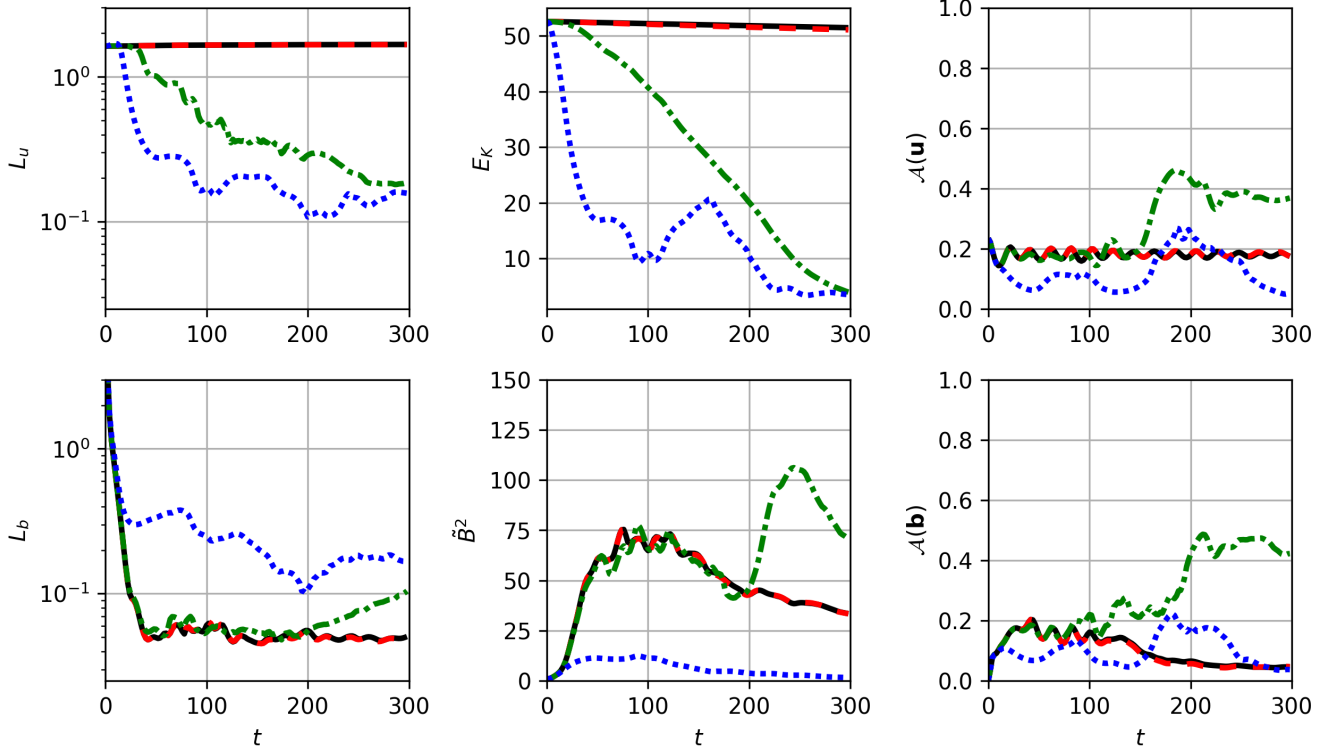


FIG. 8. Field and flow diagnostics as a function of time for case B. The four different values of M are shown as: $M = 0$ (solid black), 10^{-3} (dashed red), 10^{-2} (dot-dashed green) and 10^{-1} (dotted blue). Left column: L_u (top) and L_b (bottom). Middle column: E_K (top) and \tilde{B}^2 (bottom). Right column: $\mathcal{A}(u)$ (top) and $\mathcal{A}(b)$ (bottom).

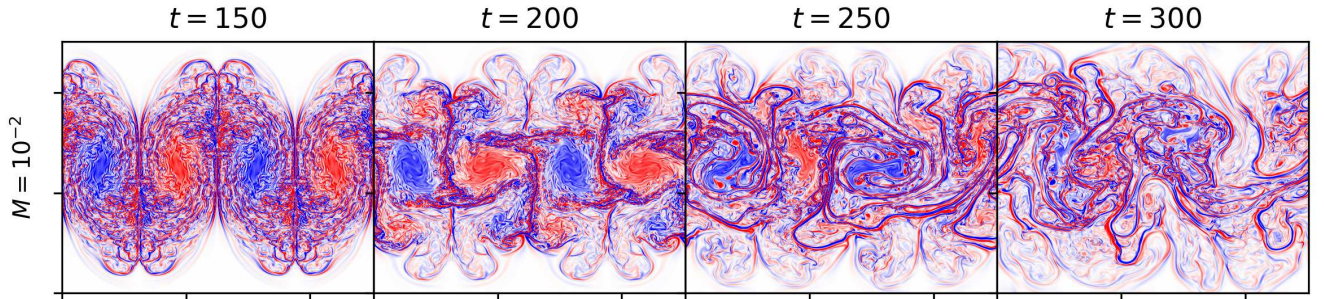


FIG. 9. Vorticity snapshots of case B for $M = 10^{-2}$, as in the third row of Fig. 6, but at longer times. The interval shown corresponds to the spike in the green curve in the magnetic field amplification (bottom right panel of Fig. 8).

- Galerkin method, in *MekIT'17 - Ninth national conference on Computational Mechanics*, edited by B. H. Skallerud and H. I. Andersson (CIMNE, 2017) pp. 273–298.
- [23] P. Godon and G. Shaviv, A two-dimensional time dependent Chebyshev method of collocation for the study of astrophysical flows, *Comput. Methods Appl. Mech. Engrg.* **110**, 171 (1993).
- [24] J. V. Shebalin, W. H. Matthaeus, and D. Montgomery, Anisotropy in MHD turbulence due to a mean magnetic field, *Journal of Plasma Physics* **29**, 525 (1983).
- [25] J. Tessier, N. Castro-Folker, F. Poulin, and M. Stastna, Anisotropy in Faraday instabilities of a shallow conducting fluid, *EPL (Europhysics Letters)* **135**, 34001 (2021).
- [26] P. Garaud, Magnetic confinement of the solar tachocline, in *The Solar Tachocline*, edited by D. W. Hughes, R. Rosner, and N. O. Weiss (Cambridge University Press, 2007).
- [27] N. Weiss, Presidential Address: Turbulent magnetic fields in the Sun, *Astronomy and Geophysics* **42**, 3.10 (2001).
- [28] D. O. Gough and M. E. McIntyre, Inevitability of a magnetic field in the Sun's radiative interior, *Nature (London)* **394**, 755 (1998).
- [29] D. O. Gough, An introduction to the solar tachocline, in *The Solar Tachocline*, edited by D. W. Hughes, R. Rosner, and N. O. Weiss (Cambridge University Press, 2007).
- [30] M. E. McIntyre, Magnetic confinement and the sharp tachopause, in *The Solar Tachocline*, edited by D. W. Hughes, R. Rosner, and N. O. Weiss (Cambridge University Press, 2007).
- [31] M. French, A. Becker, W. Lorenzen, N. Nettelmann, M. Bethkenhagen, J. Wicht, and R. Redmer, Ab initio simulations for material properties along the Jupiter adiabat, *Astrophys. J. Suppl.* **202**, 5 (2012).
- [32] M. Preising, M. French, C. Mankovich, F. Soubiran, and R. Redmer, Material properties of Saturn's interior from ab initio simulations, *Astrophys. J. Suppl.* **269**, 47 (2023).
- [33] C. A. Jones, Planetary Magnetic Fields and Fluid Dynamos, *Ann. Rev. Fluid Mech.* **43**, 583 (2011).
- [34] Y. Kaspi, E. Galanti, R. S. Park, K. Duer, N. Gavriel, D. Durante, L. Iess, M. Parisi, D. R. Buccino, T. Guillot, D. J. Stevenson, and S. J. Bolton, Observational evidence for cylindrically oriented zonal flows on Jupiter, *Nature Astronomy* **7**, 1463 (2023).
- [35] V. Zeitlin, Remarks on rotating shallow-water magnetohydrodynamics, *Nonlinear Processes in Geophysics* **20**, 893 (2013).
- [36] J. Tessier, *Jets, Vortices and Turbulence in Quasi-Geostrophic Magnetohydrodynamics*, Master's thesis, University of Waterloo (2022).
- [37] L. J. Gostelow, *Shear Flow Instabilities in Quasi-Geostrophic Shallow-Water Magnetohydrodynamics*, Ph.D. thesis, University of Leeds (2025).

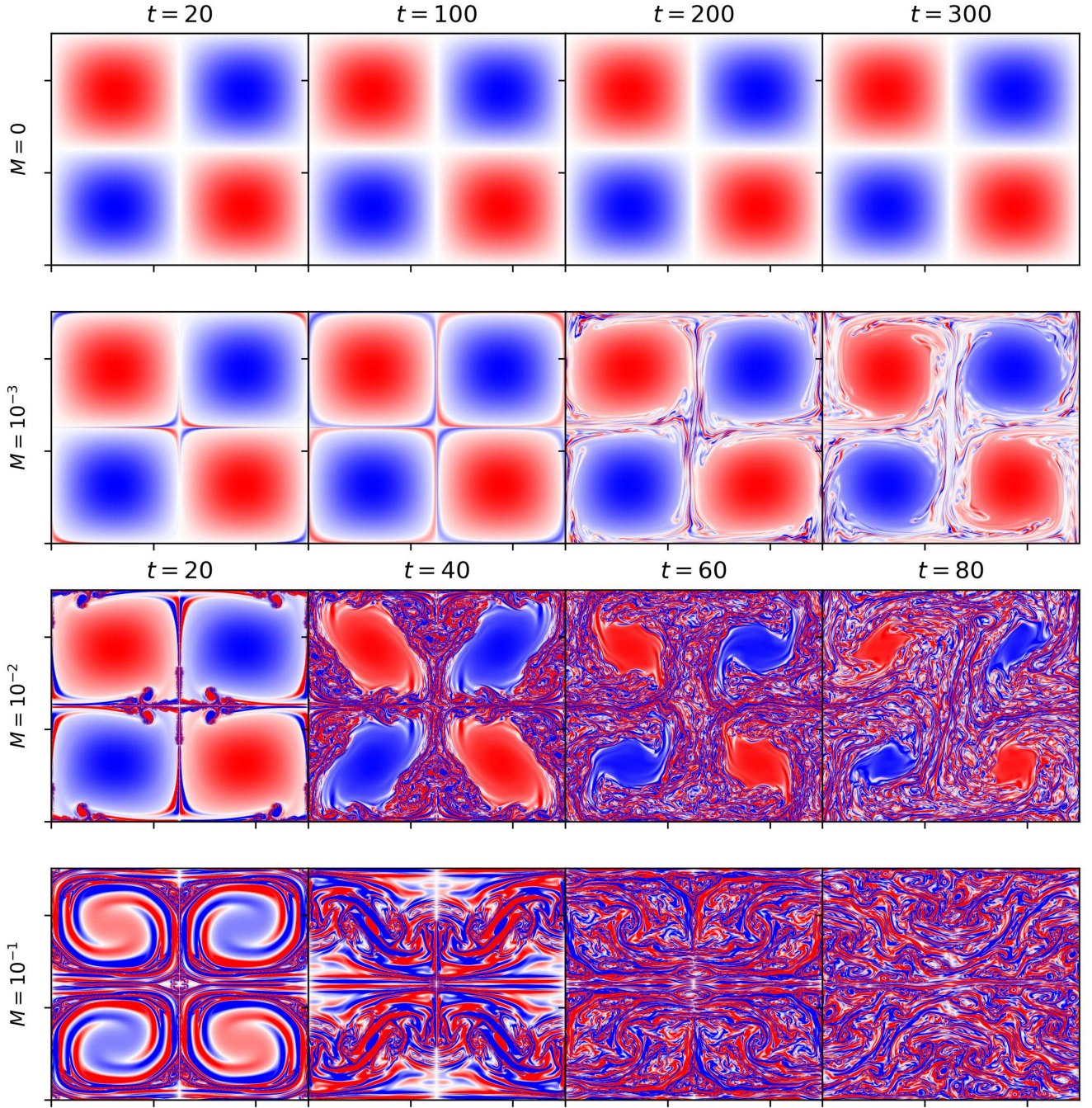


FIG. 10. Snapshots of the vorticity q for increasing $M = 0, 10^{-3}, 10^{-2}, 10^{-1}$, at times $t = 20, 100, 200, 300$ for the two smallest values of M , and at times $t = 20, 40, 60, 80$ for the two largest. The initial condition has $q = q_{tile}$ with a background magnetic field $\bar{\mathbf{b}} = \hat{\mathbf{x}}$ (case C).

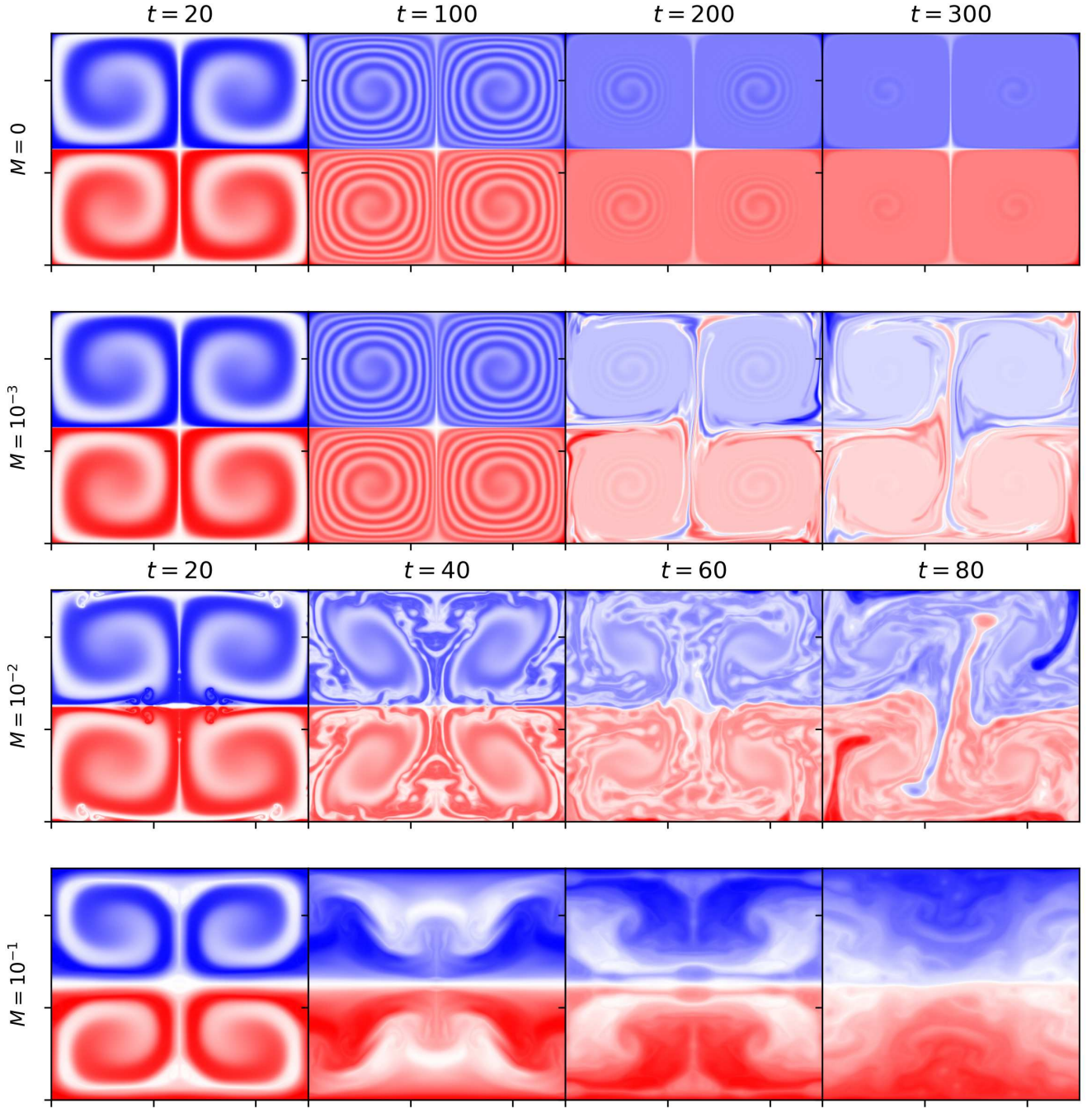


FIG. 11. Snapshots of the magnetic flux function $(\bar{A} + A)$ for increasing $M = 0, 10^{-3}, 10^{-2}, 10^{-1}$, at times $t = 20, 100, 200, 300$ for the two smallest values of M , and at times $t = 20, 40, 60, 80$ for the two largest, for case C.

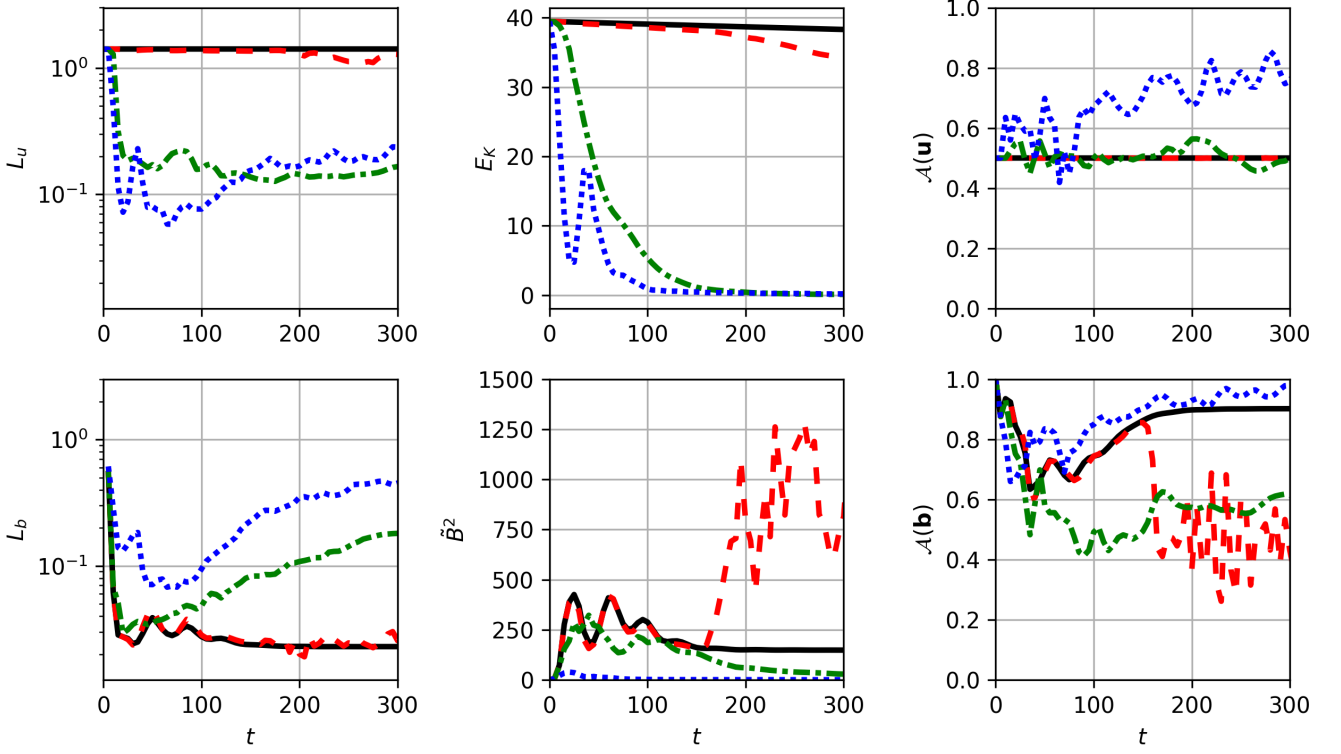


FIG. 12. Field and flow diagnostics as a function of time for case C. The four different values of M are shown as: $M = 0$ (solid black), 10^{-3} (dashed red), 10^{-2} (dot-dashed green) and 10^{-1} (dotted blue). Left column: L_u (top) and L_b (bottom). Middle column: E_K (top) and \tilde{B}^2 (bottom). Right column: $\mathcal{A}(u)$ (top) and $\mathcal{A}(b)$ (bottom).

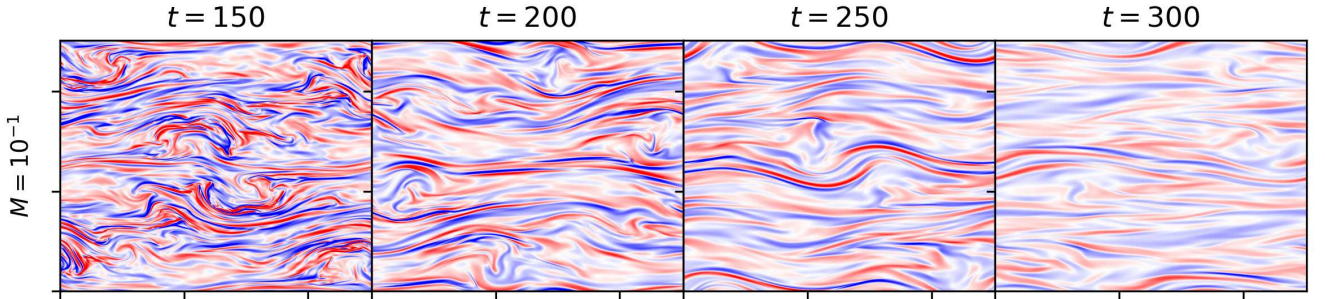


FIG. 13. Vorticity snapshots of case C for $M = 10^{-1}$, as in the fourth row of Fig. 10, but at longer times. The plots clearly show flow organization in the direction of the field; the evolution corresponds to the blue curve in $\mathcal{A}(u)$ (top left panel of Fig. 12).